Journal of
Marine Science
and Engineering

MDPI

Article

Underwater Configuration and Safe Operating Domain of a Deep-Sea Mining Vehicle–Flexible Hose System Considering Structural and Two-Phase Flow Constraints

Yan Li [1,2,*], Keping Jiang [1] and Zhibin Han [1]

1 College of Mechanical and Electrical Engineering, Central South University, Changsha 410083, China; 243711032@csu.edu.cn (K.J.); nianci95@gmail.com (Z.H.)
2 National Key Laboratory of Deep-Sea Mineral Researches Development and Utilization Technology, Changsha 410083, China
* Correspondence: yanlicsu@csu.edu.cn

Abstract

Flexible hoses connecting seabed mining vehicles to relay stations must remain suspended, limit vehicle loads, satisfy bending constraints, and maintain stable slurry transport. This study combines a lumped mass hose model, time domain vehicle motion analysis, and sequential structural-to-flow coupling with CFD–DEM to determine the safe operating domain of a 220 m single-arch hose. Thirteen buoyancy layouts were screened using seabed clearance, effective tension, curvature, and vehicle loads. Among the tested layouts, a buoyancy section extending from the vehicle end to 0.6L provided the best compromise. During outward travel, turning-induced peaks governed structural safety; after path optimization, the peak longitudinal and lateral hose loads were 17.78 and 22.38 kN, respectively, and the minimum bending radius remained above 2 m. At a reference slurry velocity of 5 m/s and solid volume fraction of 10%, a 40 m vehicle–relay spacing produced strong particle slip and concentration rebound near the lower bend, whereas 197 m promoted particle accumulation and a thicker moving bed. Integrating structural and conveying constraints yielded a recommended horizontal spacing of 80–160 m. Scaled pool tests and a published vertical pipe benchmark supported the numerical approach. The resulting domain provides a practical basis for path boundary design under the assumptions adopted here.

Keywords: deep-sea mining; polymetallic nodules; flexible hose; hose configuration; lumped mass method; CFD–DEM; safe operating domain

1. Introduction

The rapid deployment of low-carbon technologies is increasing global demand for critical minerals such as copper, cobalt, and nickel. The International Energy Agency projects that, under current policy settings, demand for copper, cobalt, and nickel in 2040 will reach approximately 1.3, 1.5, and 1.7 times the 2024 levels, respectively [1]. Against this background, deep-sea polymetallic nodules have attracted sustained attention because of their wide distribution and enrichment in multiple valuable metals [2]. Since the 1960s, several mining concepts including drag bucket, continuous rope bucket, and shuttle vehicle systems have been proposed and tested [3]. Subsequent sea trials by consortia such as OMI and OMA demonstrated the engineering feasibility of pipeline-based lifting systems [4]. Among pneumatic and hydraulic lifting concepts, hydraulic transport is generally favored for its higher conveying efficiency [5]. In a typical system, a tracked seabed mining vehicle

Check for updates

Academic Editor: Giacomo Viccione

Received: 9 August 2026
Revised: 27 August 2026
Accepted: 31 August 2026
Published: 2 September 2026

Copyright: © 2026 by the authors. Licensee MDPI, Basel, Switzerland. This article is an open access article distributed under the terms and conditions of the Creative Commons Attribution (CC BY) license.

collects nodules and transfers the slurry through a flexible hose to an underwater relay station, after which a rigid riser transports the slurry to the surface vessel [6]. The flexible hose is therefore a key interface between mobile seabed equipment and the lifting system: it must accommodate vehicle motion, remain clear of the seabed, limit loads transmitted to the vehicle, satisfy bending limits, and maintain stable internal slurry transport [7].

Distributed buoyancy is commonly used to form wave-shaped or single-arch hose configurations and to reduce direct seabed contact. Previous studies have shown that buoyancy magnitude and installation position strongly affect hose geometry, end tension, curvature, and the loads transmitted to mining vehicles [8]. Fully suspended wave configurations can reduce seabed abrasion and sediment disturbance and are therefore attractive for deep-water applications [9,10]. Wang [11] and Oh et al. [12] investigated the influence of buoyancy distribution on single-arch hose configuration and end tension. Xiao [13] established a kilometer-scale lifting system finite element model and proposed preferred initial hose configurations. Peng et al. [14] analyzed the dynamic response of flexible hoses for different operating ranges and travel paths, while Chen et al. [15] showed that vehicle speed and motion pattern can significantly alter hose configuration and vehicle loads. Fu et al. [16,17] evaluated buoyancy arrangements from the perspective of vehicle ground pressure and horizontal drag, and Song et al. [18] examined the sensitivity of hose curvature, stress, and vehicle loading to operating parameters. Zou et al. [19] analyzed flexible hose mechanics over complex terrain using the absolute nodal coordinate formulation. OrcaFlex-based studies have also been used to evaluate global tension and bending radius distributions and to support digital twin development for deep-sea lifting systems [20,21].

However, structural safety alone does not guarantee reliable slurry transport. Most hydraulic transport studies focus on vertical or inclined rigid pipes, whereas particle transport in strongly deformed flexible hoses remains less well characterized. Preliminary studies on the conveyance of solid particles in pipelines have primarily focused on the suspended flow of fine particles such as pulverized coal and sediments. Cao et al. [22] relied on extensive physical experiments to optimize conveyance parameters and thereby solve practical engineering problems. Experimental studies by Yoon et al. [23–25] demonstrated that particle size and solid volume fraction affect hydraulic gradient and pressure drop in flexible hoses. Parenteau and Lemaire [26] reported higher pressure requirements in S-shaped pipelines than in horizontal pipes, and Murai et al. [27] showed that internal flow can influence the dynamic behavior of flexible risers. Wang et al. [28] found that flow resistance is sensitive to slurry concentration, conveying velocity, and, under some conditions, buoyancy configuration. CFD–DEM studies have subsequently been used to resolve particle velocity, local concentration, and moving bed behavior in curved or flexible pipelines [29–32]. These findings indicate that hose geometry, structural response, and internal particle transport should be considered together when defining the allowable operating range of a seabed mining vehicle.

Two gaps motivate the present study. First, buoyancy layout optimization and mining vehicle path constraints are often treated separately, although vehicle motion continuously changes hose tension, curvature, and load direction. Second, internal two-phase flow safety is rarely used as an additional geometric constraint when defining the vehicle operating region. To address these gaps, a 220 m single-arch mining hose is studied using a sequential multi-model framework. Thirteen buoyancy layouts are first screened using lumped mass static and dynamic simulations in OrcaFlex. The resulting vehicle loads and minimum bending radii are used to identify the structurally feasible travel range. Centerline geometries at five representative vehicle–relay horizontal separations are then transferred to CFD–DEM models to evaluate particle velocity and local solid concentration under a reference transport condition. Finally, the structural and conveying constraints are integrated to define a distance-based safe operating domain. Scaled hose tests and a published vertical pipe benchmark are used to assess the numerical models. Waves, cross-currents, seabed undulations, and vehicle–sediment dynamic coupling are neglected; therefore, the derived domain is specific to the equipment parameters and modeling assumptions adopted here.

2. Materials and Methods

The overall research workflow is outlined as follows:

1. Thirteen buoyancy layouts are compared using a static lumped mass hose model, and configurations associated with seabed contact or negative end effective tension are excluded.
2. Time domain simulations are performed for the remaining layouts as the mining vehicle moves away from and toward the relay station; longitudinal, lateral, and vertical vehicle loads together with the minimum hose bending radius are used as structural safety criteria.
3. Centerline coordinates of five representative hose configurations are transferred from OrcaFlex to CFD–DEM models to evaluate solid–liquid transport at a reference conveying velocity and solid volume fraction.
4. The structural and conveying constraints are integrated to define a feasible horizontal-distance range and a corresponding distance-based operating domain around the relay station.

The coupling between the structural and flow models is sequential and one-way: the hose geometry obtained from OrcaFlex is used to construct the CFD–DEM flow domain, whereas the CFD–DEM results are not fed back to update hose deformation. Within the CFD–DEM solver, however, fluid–particle momentum exchange is treated through the coupled Eulerian–Lagrangian formulation. Because the environmental model is horizontally isotropic (flat seabed, fixed relay station, and no cross-current), static configurations with the same horizontal separation are equivalent under horizontal rotation. This permits the distance criterion to be represented as a first-order annular domain; actual trajectories must still satisfy the dynamic turning constraints evaluated in the time domain analysis.(Software versions used: Oracflex 11.4d, Flent 2022 R1and EDEM 2021.2).

2.1. Lumped Mass Dynamic Calculation for Flexible Hoses

The static calculation determines the equilibrium position and orientation of each hose segment and provides the initial state for subsequent time domain analysis. In the lumped mass formulation, the hose is discretized into massless straight segments connected by nodes at which mass, submerged weight, buoyancy, and hydrodynamic loads are concentrated (Figure 1). Axial, torsional, and bending responses are represented by equivalent spring–damper relationships between adjacent segments and nodes [33,34].

The nodal load calculation proceeds in five stages. First, the effective tension T_e in each segment is calculated as follows:

$$T_e = T_W + (p_o a_o - p_i a_i), \tag{1}$$

where T_w is the wall tension; p_o and p_i are the external and internal pressures, respectively; and a_o and a_i are the external and internal stress areas, respectively. Second, the bending moment $\boldsymbol{M_b}$ is calculated from

$$|\boldsymbol{M}_{\mathrm{b}}| = \boldsymbol{BM}(|c|) + d' \frac{d|c|}{dt}, \tag{2}$$

where $\boldsymbol{BM}(|c|)$ denotes the constitutive relationship between bending moment and curvature. Third, after the bending moments at the two ends of a segment have been obtained, the shear force $\boldsymbol{f}_s$ is calculated as

$$\boldsymbol{f}_s = \boldsymbol{s}_z \times \frac{1}{l}(\boldsymbol{M}_{b2} - \boldsymbol{M}_{b1}), \tag{3}$$

where $\boldsymbol{s}_z$ is the unit vector along the segment, l is the instantaneous segment length, and $\boldsymbol{M}_{b1}$ and $\boldsymbol{M}_{b2}$ are the bending moment vectors at the two segment ends. Fourth, the torsional moment M_t is calculated as

$$|\boldsymbol{M}_t| = k\,\frac{\tau_0}{l_0} + k_{tt}\,\epsilon + c\,\frac{d\tau}{dt}, \tag{4}$$

where k is the torsional stiffness, τ_0 is the segment twist angle, l_0 is the unstretched segment length, k_{tt} is the tension–torsion coupling coefficient, ϵ is the mean axial strain, c is the torsional damping coefficient, and $\frac{d\tau}{dt}$ is the twist rate.

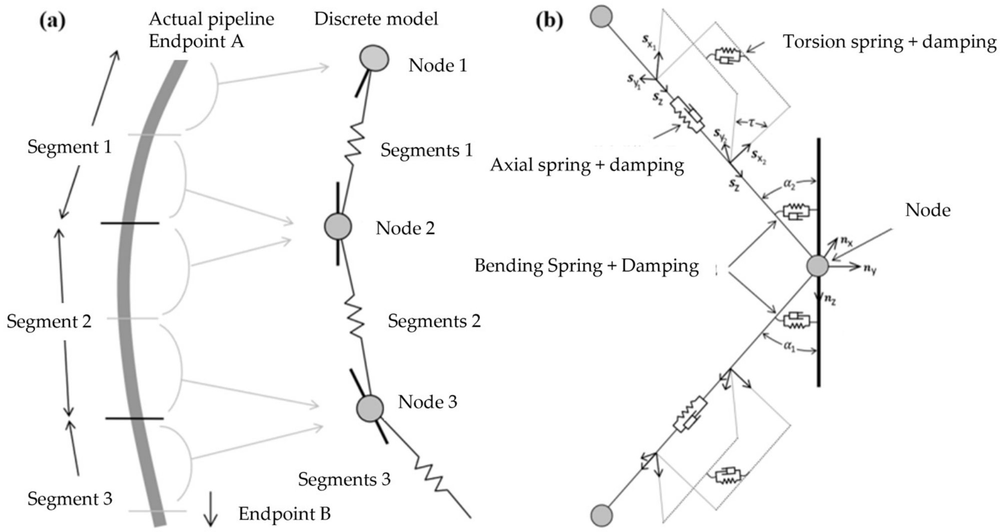

Figure 1. Lumped mass representation of the flexible hose: (**a**) physical hose and discretized line model; (**b**) equivalent spring–damper representation at a node.

2.2. Traction Resistance Analysis of Mining Vehicles

The traction demand of the tracked mining vehicle comprises internal transmission resistance and external resistance associated with seabed deformation, grade climbing, turning, hydrodynamic drag, and the flexible hose [35]. The following expressions are used to estimate the principal resistance components and to define the allowable hose-induced loads.

Seabed Soil Resistance

Soil resistance includes compression resistance and bulldozing resistance. Compression resistance is calculated as

$$\boldsymbol{R}_c = b_t \int_0^{Z_\parallel} \sigma dz, \tag{5}$$

where σ denotes the shear strength of seabed sediments (Pa), b_t represents the total width of the tracks (m) and $Z_\parallel$ represents the indentation depth (m). A simplified calculation can be performed for the compressive resistance mentioned above.

$$\boldsymbol{R}_c = b_t \cdot Z_\parallel \cdot \sigma, \tag{6}$$

Bulldozing resistance $\boldsymbol{R}_b$:

$$\boldsymbol{R}_b = 2bZ_\parallel \tau[\tan\delta + \tan(\varphi - \delta)], \tag{7}$$

where φ is the angle of internal friction of the sediment, which is approximately 3°~5°, and τ is the shear strength of seafloor sediments, which is approximately 2.5~3 kPa [35], where the relevant geometric parameter is the track entry angle.

$$\delta = arccos(1 - \frac{Z_{\parallel}}{r_d}), \tag{8}$$

Climbing Resistance:

$$\boldsymbol{F}_P = 9.8Wsin\alpha, \tag{9}$$

Turning Resistance:

The turning resistance of deep-sea tracked mining vehicles is expressed as $\boldsymbol{F}_H$:

$$\boldsymbol{F}_H = 9.8\frac{\mu WL}{2b}[1-(\frac{2e}{L})^2]^2, \tag{10}$$

where μ is the friction coefficient between tracks and deep-sea soft sediments, and μ = 0.08 [35].

Seawater Hydrodynamic Drag:

The classic drag force formula is adopted $\boldsymbol{F}_W$:

$$\boldsymbol{F}_W = \frac{1}{2}\rho K_W A V^2, \tag{11}$$

where the seawater density ρ = 1025 kg/m^3.

Flexible Hose Traction Resistance

A large horizontal pulling force will be exerted on the mining vehicle when the tensioned hose forms an inclination angle larger than 45°. In engineering design, this horizontal force $\boldsymbol{F}_G$ is generally limited to less than 10% of the total vehicle traction [35].

The total required traction is the superposition of all resistance components:

$$\boldsymbol{F}_{q\max} = \boldsymbol{R}_c + \boldsymbol{R}_b + \boldsymbol{F}_W + \boldsymbol{F}_P + \boldsymbol{F}_H + \boldsymbol{F}_G, \tag{12}$$

Travel Performance Verification

Assuming uniform ground pressure distribution on the tracks, the maximum thrust that soft seabed sediments can provide is

$$\boldsymbol{F}_{t\max} = A_2\tau(1+\frac{2h_c}{b}), \tag{13}$$

where A_2 stands for the total contact area of the tracks.

Normal travel can be guaranteed only if the following criterion is satisfied:

$$\boldsymbol{F}_{qmax} \leq \boldsymbol{F}_{tmax}, \tag{14}$$

The above condition is satisfied for the vehicle parameters used in this study. After accounting for the additional resistance of the collection head and concentration device, the maximum design traction of the travel system is 180 kN. The allowable longitudinal hose resistance is therefore set to 18 kN. For lateral stability, a static overturning check with a safety factor of 3 gives an allowable lateral hose load of 40.9 kN [35]. The vertical hose force is additionally required to remain below the available submerged normal load so that seabed contact is maintained. Together with the 2 m minimum bending radius specified for the hose, these limits form the structural screening criteria used in the subsequent path analysis.

2.3. CFD–DEM Solid–Liquid Two-Phase Governing Equations

Seawater is considered an incompressible Newtonian fluid. The fluid phase satisfies the Navier–Stokes equations for mass conservation and momentum conservation:

$$\nabla \cdot \boldsymbol{u} = 0, \tag{15}$$

$$\frac{\partial \boldsymbol{u}}{\partial t} + \boldsymbol{u} \cdot \nabla \boldsymbol{u} = -\frac{1}{\rho_f} \nabla p + v \nabla^2 u + \boldsymbol{f}_g + \boldsymbol{f}_{pf}, \tag{16}$$

where ρ_f is the liquid density, $\boldsymbol{u}$ is the liquid velocity, t is time, v is the kinematic viscosity, $\boldsymbol{f}_g$ is the gravitational acceleration, and $\boldsymbol{f}_{pf}$ is the particle–fluid momentum exchange term. Because the liquid density is assumed constant, $\frac{\partial \rho_f}{\partial t}$=0.

In the coupled CFD–DEM calculation, the translational and rotational motions of each particle are solved in the discrete element solver according to the Newton–Euler equations. At the relatively low solid concentration considered here, the dominant contributions are particle weight, interparticle contact forces, and fluid-induced forces and moments. The governing equations for an individual particle are

$$m_i \frac{d\boldsymbol{u}_i}{dt} = \boldsymbol{F}_i^{f-p} + \sum_{j=0}^{k} \left(\boldsymbol{F}_{ij}^{tp} + \boldsymbol{F}_{ij}^{np} \right) + m_i \boldsymbol{g}, \tag{17}$$

$$I_i \frac{d\boldsymbol{\omega}_i}{dt} = \sum_{j=0}^{k} \boldsymbol{M}_{ij}^{p} + \boldsymbol{M}_i^{f-p}, \tag{18}$$

where m_i, $\boldsymbol{u}_i$, I_i, and $\boldsymbol{\omega}_i$ are the particle mass, translational velocity, moment of inertia, and angular velocity, respectively; $\boldsymbol{F}_{ij}^{tp}$ and $\boldsymbol{F}_{ij}^{np}$ are the tangential and normal contact forces acting on particle i because of contact with particle j; k is the total number of particles; $m_i\boldsymbol{g}$ is the gravitational force on particle i; $\boldsymbol{M}_{ij}^{p}$ is the contact torque between particles i and j; and $\boldsymbol{M}_i^{f-p}$ and $\boldsymbol{F}_i^{f-p}$ are the fluid-induced torque and force on particle i, respectively. The principal fluid forces considered in the pipe include drag, virtual mass, pressure gradient, Magnus lift, Saffman lift, and Basset history forces. Their resultant $\boldsymbol{F}_{f-p}$ is expressed as

$$\boldsymbol{F}_{f-p} = \boldsymbol{F}_{Drag} + \boldsymbol{F}_{vm} + \boldsymbol{F}_{P} + \boldsymbol{F}_{Magnus} + \boldsymbol{F}_{Suffman} + \boldsymbol{F}_{Basset}, \tag{19}$$

2.4. Numerical Simulation Models and Working Conditions

2.4.1. OrcaFlex Lumped Mass Pipeline Model

The numerical model constructed in OrcaFlex includes tracked mining vehicle, 220 m flexible conveying hose, simplified underwater relay station and 22 discrete buoyancy modules. Seawater density is set as 1025 kg/m^3, and operating water depth equals 5000 m. Assume that the mining truck weighs 40 metric tons on land and 15 metric tons underwater, and measures 10 m long, 5 m wide, and 3 m high. Ocean waves and cross currents are excluded to isolate the independent effects of buoyancy layout and miner relay distance. Homogeneous ore slurry with equivalent density of 1126.5 kg/m^3 and bulk velocity of 5 m/s is adopted to equivalently represent steady internal flow loads (Figure 2).

The main vehicle parameters are summarized in Table 1. The travel speed is fixed at 0.5 m/s. Two motion phases are considered: movement away from and movement toward the relay station. The initial return mining path uses a 10 m minimum turning radius and a 120 m single-pass distance in the Y direction; this path is subsequently modified using the structural and internal transport constraints (Figure 3).

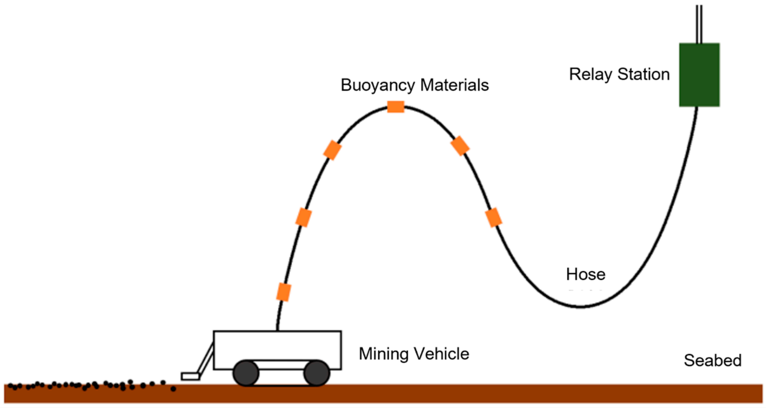

Figure 2. Schematic diagram of deep-sea mining flexible hose conveying system.

Table 1. Main design parameters of the tracked deep-sea mining vehicle.

Parameter	Value
Mass in air	40 t
Equivalent submerged mass	15 t
Longitudinal center-of-gravity offset	0.1 m
Projected frontal area	15 m^2
Sinkage, ZII	0.2 m
Mean ground pressure	6.57 kPa
Track width, b	1.6 m
Ground contact length per track, l	7 m
Travel speed, V	0.5 m/s
Maximum grade angle, α	10°
Minimum turning radius	10 m
Maximum negotiable obstacle height	0.5 m
Maximum negotiable obstacle width	1 m
Longitudinal track inclination	2°
Track gauge	3.4 m
Grouser height, hc	0.12 m
Front-wheel outer radius, rd	0.52 m

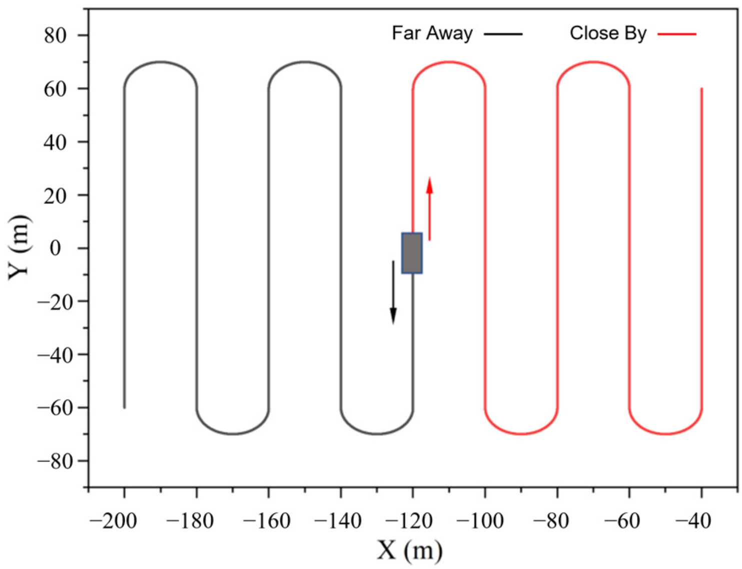

Figure 3. Schematic of initial planned mining travel path (black: miner moving away; red: miner approaching).

The hose has a total length of 220 m and is discretized into 440 uniform segments of 0.5 m, resulting in 441 nodes. End A is rigidly connected to the mining vehicle at (0,0,3) m in the vehicle-fixed coordinate system. The end fitting orientation is prescribed by azimuth = 0°, declination = 0°, and gamma = 0°, such that the local end fitting axes are initially aligned with the vehicle-fixed coordinate axes and the hose no-moment direction Ez is aligned with the vehicle local +Z direction. Infinite bending stiffness is specified about both local transverse axes, corresponding to a rigid bending connection. Torsion is not included in the present line model. End B is rigidly connected to the relay station at a height of 60 m above the seabed. The seabed is modeled as flat, and an elastic contact model is adopted for hose–seabed interaction.The hose specifications are shown in Table 2, and the definition of the buoyancy module arrangement along the hose is shown in Figure 4.

Table 2. Mechanical parameters of flexible conveying hose.

Parameter	Value
Length	220 m
Inner diameter	232 mm
Outer diameter	332 mm
Mass per unit length in air	75 kg/m
Drag coefficient	1.2
Axial drag coefficient	0.008
Added mass coefficient	1.0
Axial added mass coefficient	0
Bending stiffness	150 kN·m^2
Torsional stiffness	3430 kN·m^2/°
Tensile stiffness	28,000 kN/m
Minimum bending radius	2 m

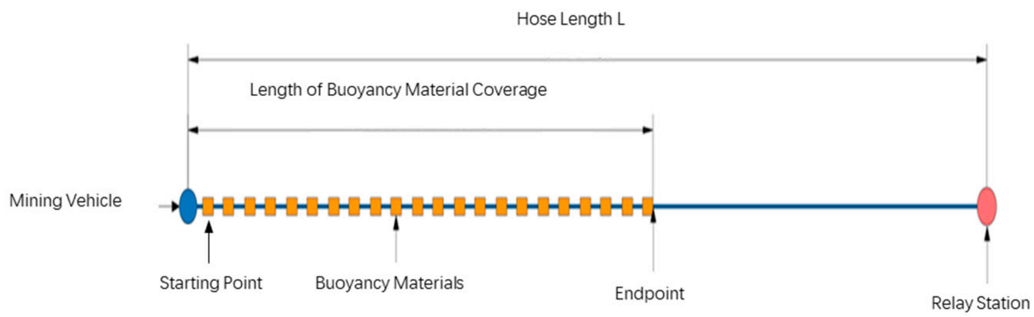

Figure 4. Definition of the buoyancy module arrangement along the hose.

The buoyancy material is configured in the "Attachment" submodule of the "Line" object; adjust the weight and volume to achieve the desired buoyancy. If the buoyancy material provides excessive buoyancy, the local bending radius of the hose may fall below the permissible limit; conversely, if the buoyancy is too low, it will fail to provide effective support for the hose. Typically, the buoyancy provided by the material is set to 0.9–1.1 times the hose's weight. Therefore, in this study, the density of the buoyancy material is set to 0.578 g/cm^3, with a single unit weighing 438 kg and having a volume of 0.758 m^3, providing approximately 339 kg of net buoyancy. A total of 22 identical buoyancy modules were uniformly distributed within the prescribed buoyancy section for each layout. For a buoyancy section extending from S_0 to $S_0 + L_b$, the modules were positioned at equal arc length intervals $\Delta S = L_b/N_b$, where $N_b = 22$. Accordingly, the arc length coordinate of the i-th module was $S_i = S_0 + i\Delta S$ (i = 1,. . .,22). the buoyancy module layout options are shown in Table 3. For example, in Scheme 11, $L_b = 0.6L = 132$ m, giving $\Delta S = 6$ m and module positions of 6, 12, . . ., 132 m from End A. Thus, only the coverage length and starting position of the buoyancy section were varied among the 13 schemes, while the number and physical properties of the buoyancy modules remained unchanged.

https://doi.org/10.3390/jmse14171628

Table 3. Buoyancy module arrangement schemes.

Scheme	Buoyancy Section Length	Start Position	End Position
1	1/4L	0	1/4L
2	1/4L	1/4L	1/2L
3	1/4L	1/2L	3/4L
4	1/3L	0	1/3L
5	1/3L	1/3L	2/3L
6	2/5L	0	2/5L
7	2/5L	1/5L	3/5L
8	2/5L	2/5L	4/5L
9	1/2L	0	1/2L
10	1/2L	1/4L	3/4L
11	3/5L	0	3/5L
12	2/3L	0	2/3L
13	3/4L	0	3/4L

2.4.2. CFD–DEM Coupling Two-Phase Flow Model

Centerline coordinate data exported from OrcaFlex are imported into CATIA for three-dimensional geometric reconstruction of the hose fluid domain (Figure 5). Polyhedral unstructured meshes are adopted, with five layers of prismatic boundary layers arranged along pipe walls at a growth rate of 1.2. To improve model convergence and conserve computational resources, the SIMPLE solver is used to calculate the flow field inside the pipe. When performing a coupled simulation with Fluent and EDEM, to ensure proper data exchange between the software packages, Fluent's time step must be an integer multiple of EDEM's time step. In EDEM, the time step is typically set to 20–30% of the Rayleigh time step; therefore, the EDEM time step was set to 10^{-4} s, and the Fluent time step to 5×10^{-3} s. Eleven monitoring sections with 0.5 m axial length are evenly distributed along the hose to extract real-time particle velocity and local solid volume fraction data.

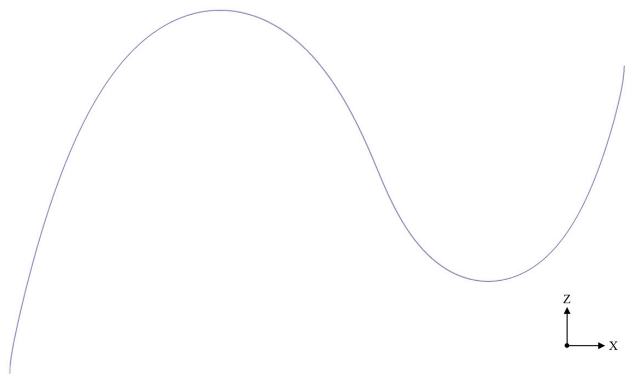

Figure 5. Two-dimensional X–Z geometric profile of single-arch flexible hose for CFD simulation.

The hose inner reinforcement layer is represented as stainless steel with a wall material density of 7800 kg/m^3 in EDEM. Irregular polymetallic nodules are simplified as monodisperse spherical particles with a diameter of 20 mm. These dimensions are commonly used settings for CFD-DEM simulations of deep-sea mining [36]. Particle density and elastic properties are based on the nodule parameters used in the thesis, and the contact parameters are taken from published data [37] (Table 4).

Particles are generated in EDEM using a cylindrical generation region located 5 m downstream of the fluid inlet. The generation region is 1 m long and has a diameter slightly smaller than the pipe diameter, providing sufficient space for stable particle insertion at the prescribed inlet concentration. A particle removal plane is placed near the pipe outlet, and the Remove_particle.dll routine is used to remove particles after they leave the fluid domain, thereby avoiding unnecessary particle tracking outside the pipe and reducing computational cost.

Table 4. Physical and contact parameters of polymetallic nodule particles.

Category	Parameter	Value
Single particle	Shape	Sphere
	Diameter	20 mm
	Density	2040 kg/m^3
	Shear modulus	21.3 MPa
	Poisson's ratio	0.40
Particle–particle contact	Restitution coefficient	0.55
	Static friction coefficient	0.50
	Rolling friction coefficient	0.10
Particle–wall contact	Restitution coefficient	0.48
	Static friction coefficient	0.10
	Rolling friction coefficient	0.01

The transient fluid phase is solved in double precision using the pressure-based solver, the realizable \(k\)–\(\varepsilon\) turbulence model, and SIMPLE pressure–velocity coupling. A velocity inlet and pressure outlet are prescribed at the pipe ends. The inlet turbulence intensity and turbulent viscosity ratio are set to 5% and 10, respectively. Standard wall functions are employed, with resulting y^+ values ranging from 127.25 to 223.12. Particle contacts are modeled using the Hertz–Mindlin model. Seawater is specified as the continuous phase with a density of 1025 kg m^{-3}. The enabled fluid force models include the Gidaspow drag correlation, Saffman lift, virtual mass force, and pressure gradient force, with the virtual mass coefficient set to 0.5. Particle rotation is enabled throughout the coupled calculation.

The total pipeline pressure drop does not show monotonic convergence with mesh refinement, which is occasionally observed for complex curved two-phase flow simulations. Although the pressure drop difference between M3 and M4 is only 0.90%, this global integral indicator alone is not sufficient for judging mesh independence, since the main conclusions of this paper rely on local flow quantities. Therefore, the local solid concentration ratio c_{pl}/c_0 at monitoring section M8 (lower bend region) is supplemented as an auxiliary convergence metric. The relative change of c_{pl}/c_0 drops to 1.3% from M3 to M4. Balancing computational cost and local field accuracy, mesh M3 (2,450,292 cells) is adopted for subsequent simulations (Table 5). Figure 6 shows the representative axial fluid velocity field for a bulk velocity of 5 m/s.

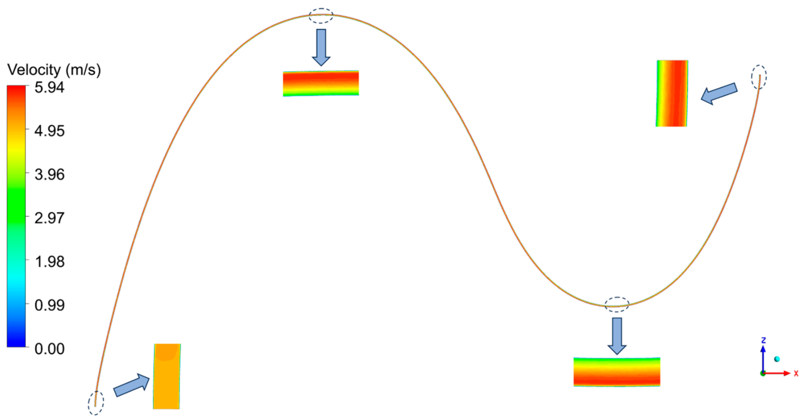

Figure 6. Axial fluid velocity contour of single-arch hose at bulk velocity of 5 m/s, with sectional sampling windows at key monitoring positions.

Table 5. Mesh independence test results of CFD fluid domain.

Mesh Group	Total Mesh Count	Pipeline Pressure Drop (kPa)	Relative Variation vs. Previous Group	M8 Section c_{pl}/c_0	Relative Variation of c_{pl}/c_0
M1	1,466,827	135.0	/	1.271	/
M2	1,865,574	131.2	−2.81%	1.182	−7.00%
M3	2,450,292	133.0	1.37%	1.153	−2.45%
M4	3,351,699	134.2	0.90%	1.138	−1.30%

3. Results and Discussion

3.1. Static Geometric Analysis Under Different Buoyancy Layouts

The 13 buoyancy layouts produce markedly different static configurations (Figure 7). When the buoyancy section starts at the mining vehicle end and covers less than 0.5L (Schemes 1, 4, and 6), the upward support is insufficient to keep the entire hose clear of the seabed. By contrast, when the buoyancy section is shifted too far toward the relay station (Schemes 3 and 8), the effective tension at both ends becomes negative, indicating axial compression, and the local end curvature increases to approximately 0.4 m^{-1}. Both conditions are undesirable for long-term hose operation.

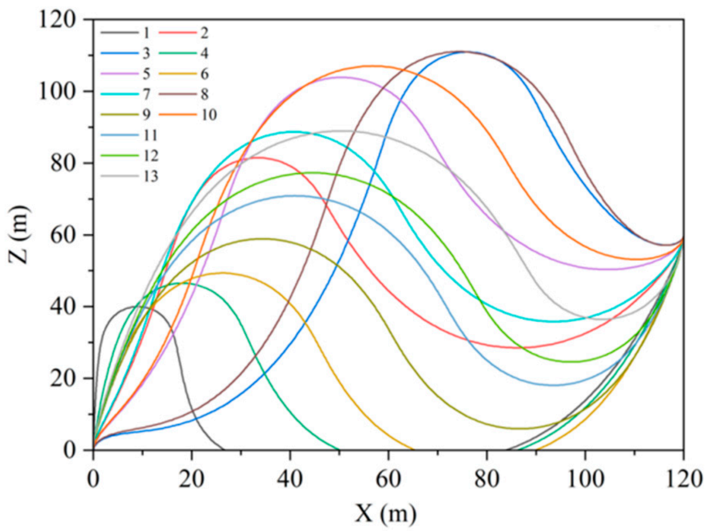

Figure 7. Static Z-height profiles of flexible hoses under 13 buoyancy layout schemes (X = horizontal distance from mining vehicle).

Increasing the buoyancy section length lowers the arch crown curvature but increases the curvature of the lower bend; Schemes 9 and 11 show comparatively balanced curvature distributions. Shifting the buoyancy section toward the relay station raises the arch and reduces the load transmitted to the vehicle, but it also increases end curvature and can drive the end effective tension into compression. Table 6 quantifies this trade-off. For layouts beginning at the vehicle end, the hose load on the vehicle decreases from 43.16 to 11.89 kN as the buoyancy coverage increases from 0.25L to 0.75L. For the 0.25L group, moving the buoyancy section toward the relay station reduces the vehicle load from 43.16 to 7.91 kN, but changes the end effective tension from positive values to approximately −2.7 kN. Accordingly, minimum vehicle load alone is not a sufficient optimization objective. After excluding seabed contact and axial compression cases, Scheme 11 (buoyancy from 0 to 0.6L) is selected as the preferred compromise among the tested layouts because it maintains full suspension, positive end effective tension, a balanced curvature distribution, and moderate vehicle loading.

Table 6. Mining vehicle traction load and terminal effective tension under all static buoyancy schemes.

Scheme	Vehicle Load (kN)	End A Tension (kN)	End B Tension (kN)
1	43.16	43.14	29.07
2	19.21	17.60	17.58
3	7.91	−2.68	−2.70
4	34.52	34.22	28.44
5	10.54	7.73	7.71
6	29.87	29.39	27.57
7	15.28	13.96	13.97
8	6.41	−2.43	−2.45
9	24.33	23.81	23.79
10	7.38	5.03	5.01
11	19.36	18.95	18.93
12	15.90	15.52	15.50
13	11.89	11.65	11.64

It should be noted that Scheme 11 (0–0.6 L buoyancy coverage) is identified as optimal under the baseline parameters of this manuscript (220 m hose length; total net buoyancy equal to the submerged hose weight). Its performance will change when key design parameters are varied. Longer hoses will transmit higher pulling loads to the mining vehicle and may exceed traction limits. Insufficient total buoyancy brings the risk of seabed contact. Hence this buoyancy layout cannot be directly copied for arbitrary hose dimensions. For other hose specifications, the full screening workflow proposed in this paper should be repeated to obtain suitable buoyancy arrangements.

3.2. Dynamic Mechanical Characteristics During Miner Travel

The hose force acting on the vehicle is resolved in the local vehicle coordinate system into longitudinal, lateral, and vertical components (Figure 8). The longitudinal component is compared with the 18 kN traction resistance limit, the lateral component with the 40.9 kN anti-overturning limit, and the vertical component with the available submerged normal load. Hose bending is evaluated against the specified minimum bending radius of 2 m.

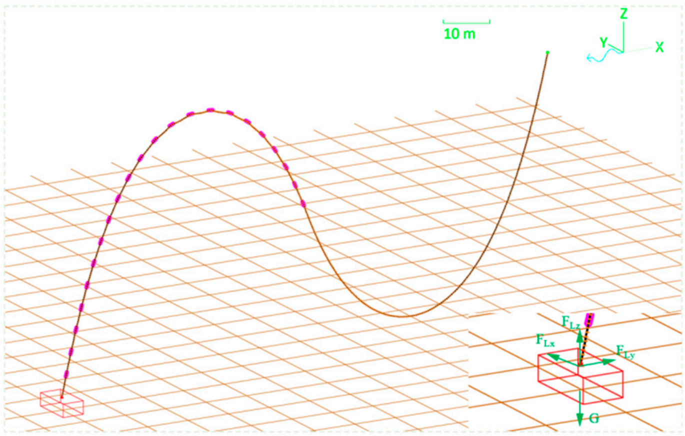

Figure 8. Decomposition of the hose load in the local mining vehicle coordinate system.

3.2.1. Working Condition: Miner Moving Away from Relay Station

As the vehicle moves away from the relay station, the longitudinal, lateral, and vertical hose loads generally increase with horizontal separation. During straight travel, the hose load components vary relatively gradually (Figure 9). During turning, however, the vehicle-fixed coordinate system rotates rapidly with the vehicle heading, whereas the spatial direction of the hose-end force cannot adjust instantaneously. Consequently, the projection of the hose force onto the vehicle longitudinal and lateral axes changes abruptly, producing pronounced peaks in the corresponding load components. At large vehicle–relay separations, the increasingly tensioned hose has less geometric compliance, further amplifying this load redistribution during turning. At Stage 6, several buoyancy layouts exceed the 18 kN longitudinal limit; by Stage 8, all retained layouts exceed the longitudinal limit and the 40.9 kN lateral criterion.

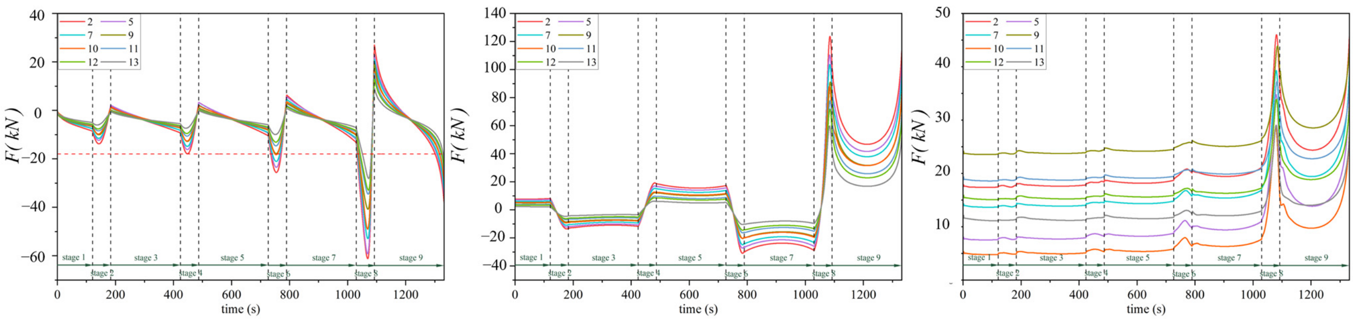

(a) Direction of travel (b) Lateral (c) Vertical direction

Figure 9. Time histories of hose-induced vehicle loads while the mining vehicle moves away from the relay station. (**a**) Direction of travel; (**b**) Lateral; (**c**) Vertical direction.

During outward travel, the hose-end connections become the critical bending locations. At Stage 8, the minimum bending radius falls below 2 m for all retained layouts. Layouts in which buoyancy is concentrated closer to the vehicle generally maintain larger end bending radii than layouts shifted toward the relay station (Figure 10).

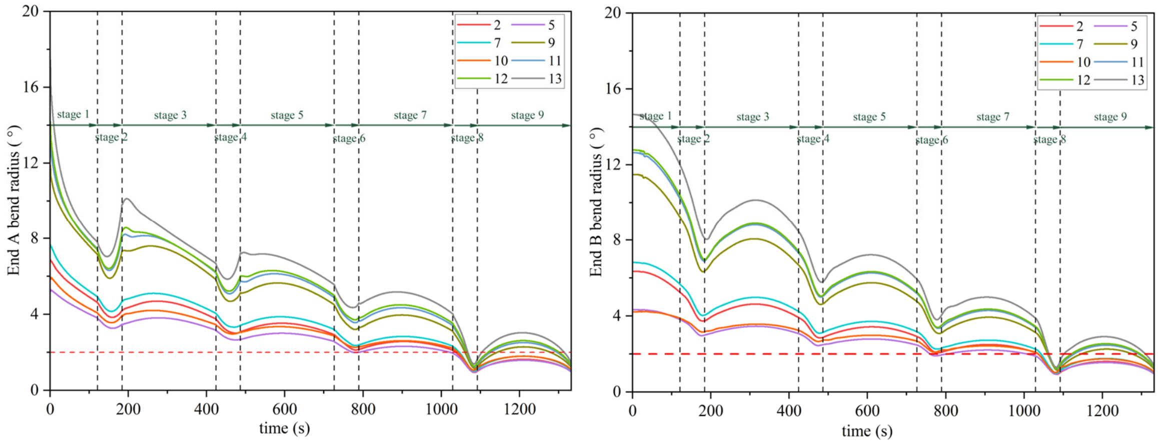

Figure 10. Time evolution of minimum bending radius at pipeline terminals during outward travel.

3.2.2. Working Condition: Miner Approaching Relay Station

As the vehicle approaches the relay station, the hose becomes progressively more relaxed, and the amplitudes of all three load components decrease. The longitudinal and lateral loads remain within their allowable limits throughout this phase. The critical bending locations shift from the hose ends to the arch crown and lower bend, but the minimum bending radii remain above 2 m for all retained layouts (Figures 11 and 12).

Comparative dynamic analysis indicates that the outward travel stage represents the high-risk working condition of the whole system. Arranging buoyancy modules adjacent to the mining vehicle side reduces multi-directional vehicle loads and increases the pipeline entry inclination angle, stabilizing particle inflow at the hose inlet. Extending buoyancy coverage effectively cuts vehicle traction loads but raises arch crown height and lowers overall effective tension; previous research proves higher effective tension improves long-term geometric stability of hoses [38]. Balancing mining vehicle traction, hose effective tension, bending radius and arch elevation, Scheme 11 (0–0.6Lbuoyancy coverage) is selected as the optimal layout.

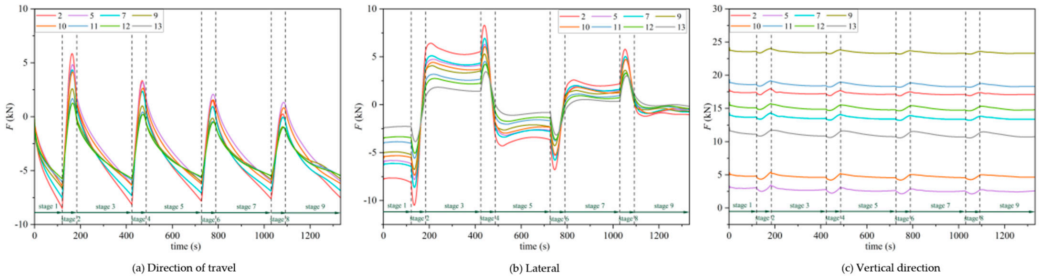

Figure 11. Time history loads on mining vehicle when approaching relay station. (**a**) Direction of travel; (**b**) Lateral; (**c**) Vertical direction.

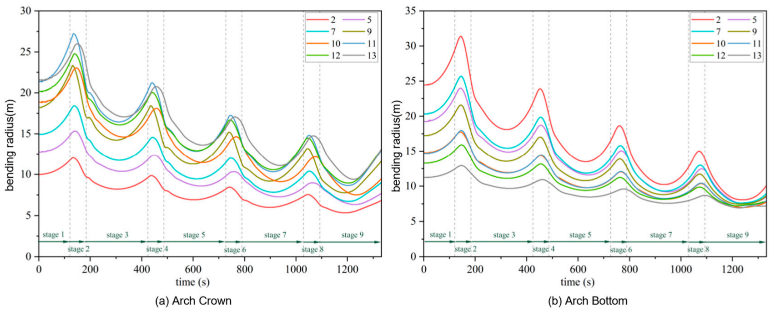

Figure 12. Time evolution of bending radii at arch crown and bottom during inward travel.

3.3. Influence of Hose Spatial Geometry on Solid–Liquid Two-Phase Flow

Five hose geometric configurations corresponding to horizontal miner relay distances of 40 m, 80 m, 120 m, 160 m and 197 m are imported into CFD–DEM models. The inclination angle of 11 axial monitoring cross-sections under each configuration is listed in Table 7. With rising horizontal spacing, the first ascending segment and middle descending segment become gentler, and vertical elevation difference between arch crown and arch bottom decreases. Simulations are carried out at bulk transport velocity of 5 m/s and solid volume fraction of 10%.

Table 7. Inclination angle (°) of 11 monitoring sections under five miner relay horizontal spacings.

Monitor	Inclination (°)				
	40	**80**	**120**	**160**	**197**
M1	89.69	82.98	73.36	59.16	36.61
M2	89.62	79.15	65.40	48.22	28.18
M3	83.76	64.17	45.5	29.68	18.23
M4	−6.90	−3.89	−0.80	2.56	7.77
M5	−84.87	−65.33	−45.13	−24.70	−3.08
M6	−89.63	−79.31	−65.15	−45.24	−14.87
M7	−87.16	−73.09	−56.47	−35.89	−9.08
M8	−4.24	−2.63	−0.41	2.57	7.64
M9	85.32	70.58	54.62	37.93	22.47
M10	89.72	81.91	71.14	55.98	33.87
M11	90.00	90.00	90.00	90.00	90.00

Taking the 120 m spacing case as an example, fluid velocity contours at all monitoring positions are displayed in Figure 13. In ascending segments M2 and M10, solid particles accumulate at the pipe bottom with lower velocity than the carrier fluid. Following the minimum flow resistance principle, high-speed fluid concentrates at the upper pipeline region. In descending segment M6, particles move faster than seawater, generating high-velocity flow near the pipe bottom. At arch crown M4 and arch bottom M8, flow patterns inherit upstream characteristics: fluid kinetic energy converts to gravitational potential energy at the crown with reduced overall velocity, while the arch bottom presents opposite flow behavior. Flow stratification gradually weakens at vertical outlet M11 with uniform particle dispersion. Contours of other spacing cases show similar distribution features and are not repeated herein.

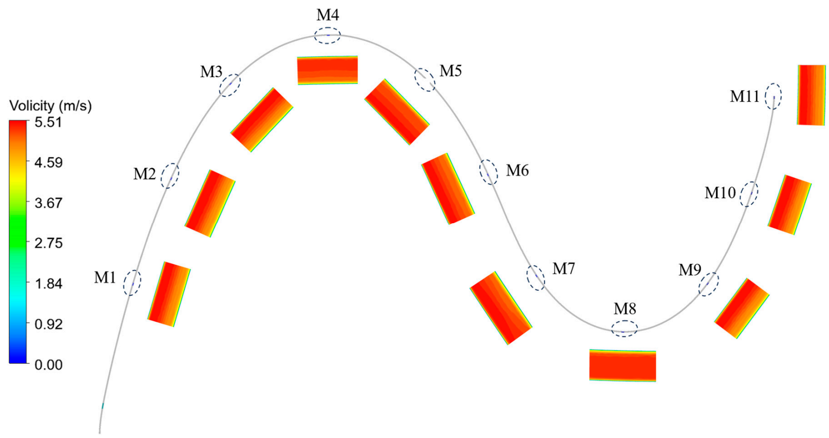

Figure 13. Schematic layout of 11 flow monitoring sections on single-arch flexible hose with fluid velocity sampling windows.

A clear gravitational slip pattern is observed: particles lag behind the carrier fluid in ascending sections but can move faster than the fluid in descending sections. In the compact 40 m configuration, the steep descending segment increases the streamwise component of gravity acting on the particles. The particles therefore accelerate before entering the lower bend, where the abrupt change in pipe orientation promotes particle–wall and particle collisions and causes rapid deceleration. As the vehicle–relay separation in-creases, the hose becomes flatter, reducing the streamwise gravitational component in the descending section. Meanwhile, the gentler ascending sections increase particle residence time near the lower wall and enhance the influence of wall friction. These effects promote persistent moving bed formation at the larger separations. Among the five tested configurations, the 120 m case exhibits the smallest overall variation in particle velocity (Figure 14).

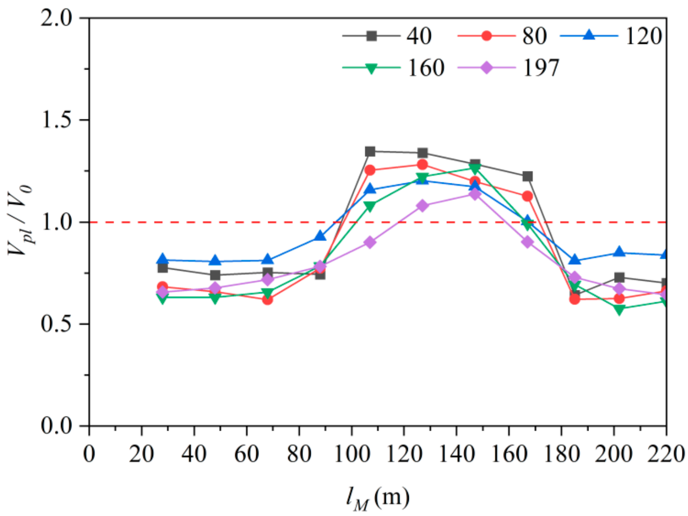

Figure 14. Axial distribution of particle velocity ratio V_{pl}/V_0 along hose length under five miner relay horizontal distances (L_M = axial distance from hose inlet).

Using a spacing of 120 m as an example, particle velocity contour plots for different monitoring locations are presented (Figure 15). Based on the subsequent analysis, velocity contour plots for other operating conditions are similar and will not be listed individually. Local solid volume fraction ratio c_{pl}/c_0 presents opposite variation trends against particle velocity: higher values in ascending segments and lower values in descending segments (Figure 16). The 40 m high-curvature compact hose triggers severe local concentration rebound at the arch bottom after high-speed particle inflow. The 197 m flat configuration generates thick particle moving beds in the first ascending segment with significant solid accumulation due to insufficient gravitational acceleration in descending sections. Fluctuation amplitudes of particle concentration under 80 m and 160 m spacing remain within acceptable ranges, while the 120 m case achieves minimum overall concentration oscillation. Under the reference transport working condition, the optimal horizontal spacing between mining vehicle and relay station is constrained within 80–160 m from the perspective of internal two-phase flow stability.

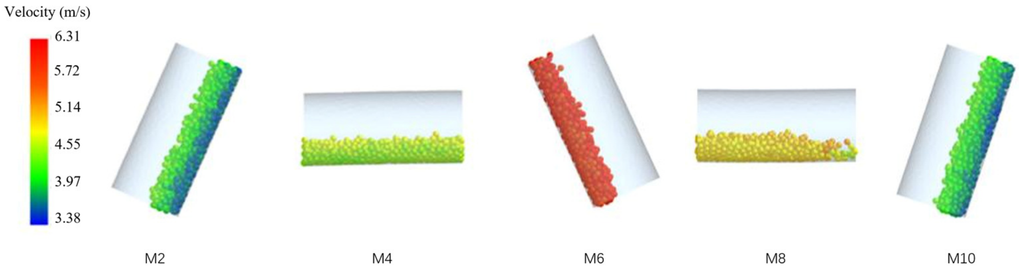

Figure 15. Particle velocity contour plots at different monitoring locations spaced 120 m apart.

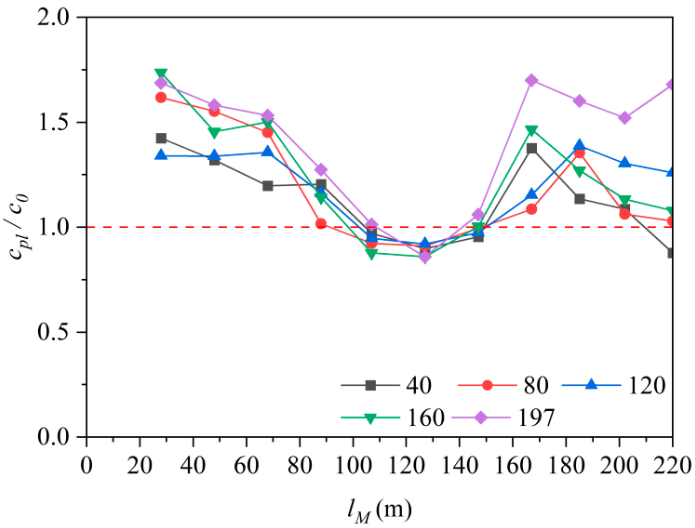

Figure 16. Axial distribution of local solid concentration ratio c_{pl}/c_0 along hose length under five miner relay horizontal distances (L_M= axial distance from hose inlet).

In summary, the relative horizontal distance between mining vehicle and relay station drastically alters hose spatial geometry, leading to distinct solid–liquid two-phase transport behaviors inside the pipeline. For the equipment and transport parameters adopted in this research, the recommended safe horizontal spacing between miners and underwater relay stations ranges from 80 m to 160 m.

3.4. Determination of Mining Vehicle Safe Operation Zone Under Coupled Dual Constraints

The initial travel path is first modified to avoid regions that violate the longitudinal traction limit, lateral stability limit, or minimum bending radius (Figure 17). The maximum single-pass distance in the Y direction is increased to 160 m in the revised path while maintaining the required turning radius. Time domain simulation of the revised path gives a maximum total hose force of 32.26 kN. The peak longitudinal, lateral, and vertical components are 17.78, 22.38, and 22.44 kN, respectively; the first two remain below their allowable limits, and the vertical component remains well below the vehicle submerged normal load. The minimum bending radii at End A, End B, the arch crown, and the lower bend all remain above 2 m (Figures 18 and 19). The critical bending location shifts from the crown/lower bend at short separation to the hose ends at large separation, which is useful when selecting locations for structural monitoring.

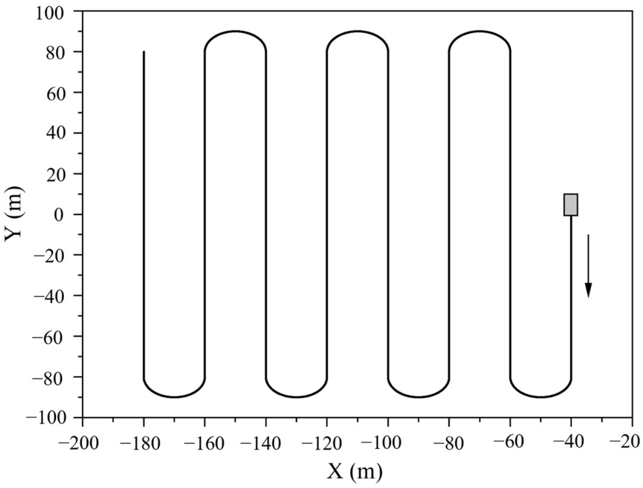

Figure 17. Optimized full travel path of deep-sea mining vehicle after structural constraint screening.

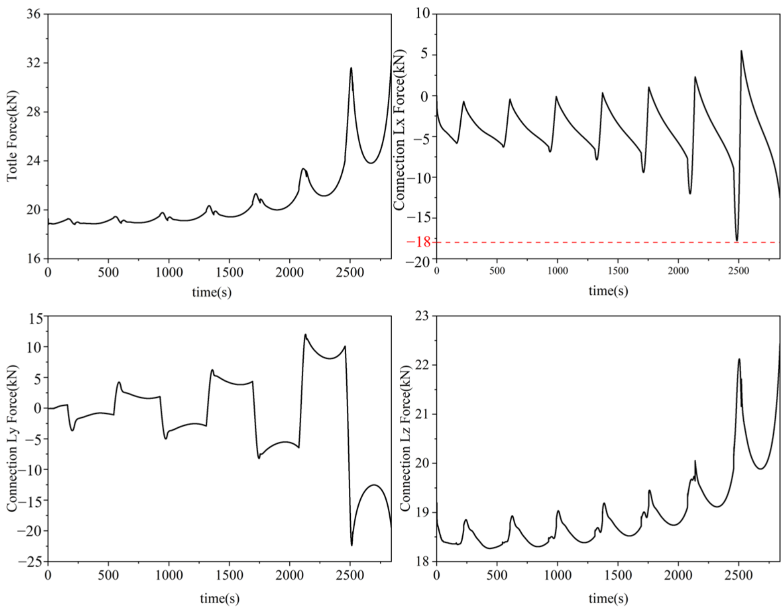

Figure 18. Time history curves of total hose traction, longitudinal, lateral and vertical loads on mining vehicle along optimized travel path.

The final distance-based operating domain is obtained by intersecting the structural and conveying constraints. The outer boundary of 160 m is governed primarily by the growth of vehicle loads and the reduction in hose-end bending radius at large separation. The inner boundary of 80 m excludes the compact, high-curvature configurations associated with large particle slip and strong concentration rebound near the lower bend. Under the flat seabed, no cross-current, horizontally isotropic assumptions, this 80–160 m interval can be rotated about the relay station to form a first-order annular feasible domain (Figure 20).

The annulus is not, by itself, a complete path guarantee: vehicle heading, turning events, and transient loads must still be checked for any specific trajectory.

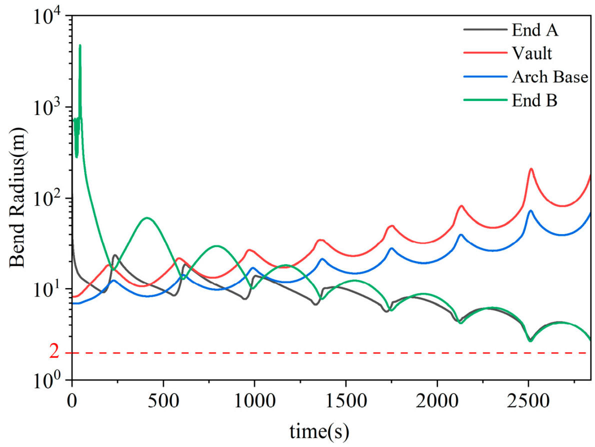

Figure 19. Minimum bending radii at End A, End B, the arch crown, and the lower bend along the revised path (red dashed line: 2 m limit).

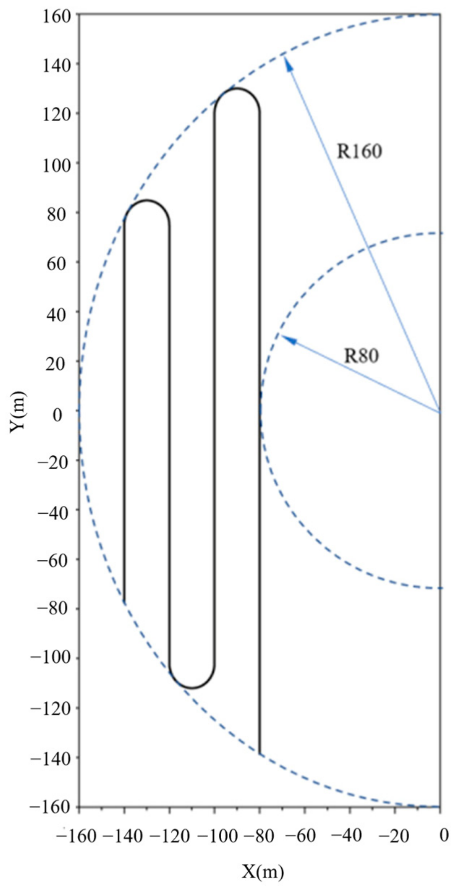

Figure 20. Distance-based annular operating domain for the present model (inner radius: 80 m; outer radius: 160 m).

4. Experimental Validation

4.1. Scaled Pool Test for Hose Geometric Configuration

A 1:100 geometric scaled water tank test platform is constructed to validate the capacity of the lumped mass numerical model to reproduce hose geometric variations induced by buoyancy layout and miner relay distance. This test only serves for qualitative trend verification instead of complete full-scale deep-sea dynamic similarity assessment (Figure 21).

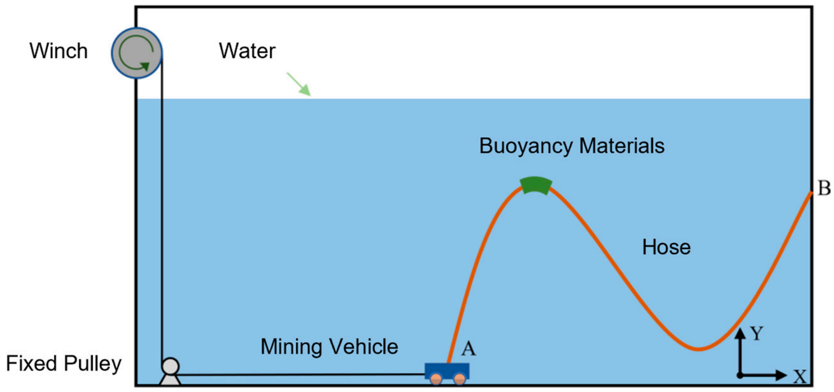

Figure 21. Schematic diagram of 1:100 scaled water tank experimental setup for flexible hose configuration test.

The transparent glass tank is 8 m long, 1.5 m wide, and 1.5 m high, with an 18 mm wall thickness; the water depth is maintained at 0.9 m. End B of the scaled hose is fixed 0.65 m above the tank bottom, and End A is connected to a scaled mining vehicle model that is translated horizontally by a winch. The test hose is a 2.2 m long PVC steel wire tube with an inner diameter of 10 mm, outer diameter of 15 mm, and linear mass density of 0.145 kg/m. Cubic buoyancy blocks with a 20 mm × 20 mm cross-section are installed at three representative positions (Figure 22 and Table 8).

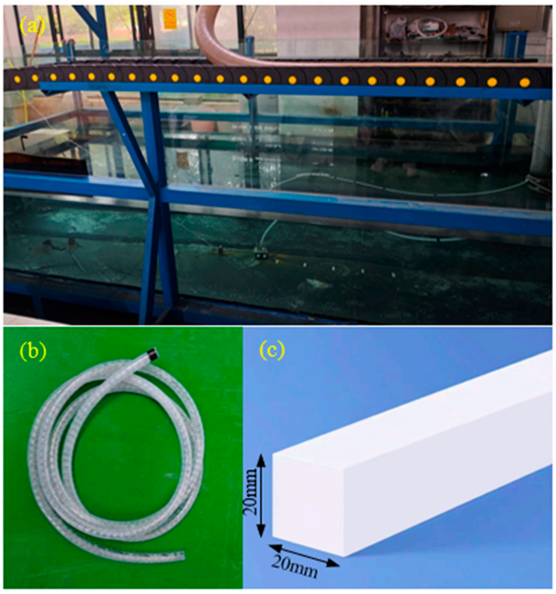

Figure 22. Main experimental components of scaled pool test: (**a**) overall glass water tank; (**b**) PVC scaled flexible hose; (**c**) cubic buoyancy module.

Table 8. Three buoyancy block layout schemes for scaled test hose (distance from End A).

Scheme	Distance from End A (cm)
1	55
2	73
3	88

4.1.1. Development of the Simulation Model

A matched numerical model is built in OrcaFlex with identical geometric and mechanical parameters as the scaled experimental hose for comparative analysis (Figure 23).

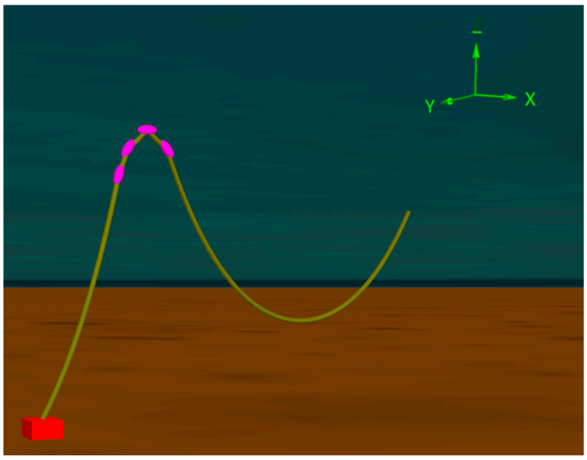

Figure 23. OrcaFlex model corresponding to the scaled water tank experiment.

4.1.2. Comparative Analysis of Experimental and Simulated Geometries

For buoyancy Scheme 1 with horizontal miner relay distance of 1.2 m, the average absolute error of vertical coordinate at 10 sampling points equals 0.034 m, root mean square error reaches 0.048 m, and maximum single-point absolute error is 0.10 m. X-coordinates are preset fixed sampling positions and excluded from error evaluation. With increasing horizontal spacing, the arch crown height declines and arch bottom elevation rises, with the hose overall flattening gradually (Figure 24).

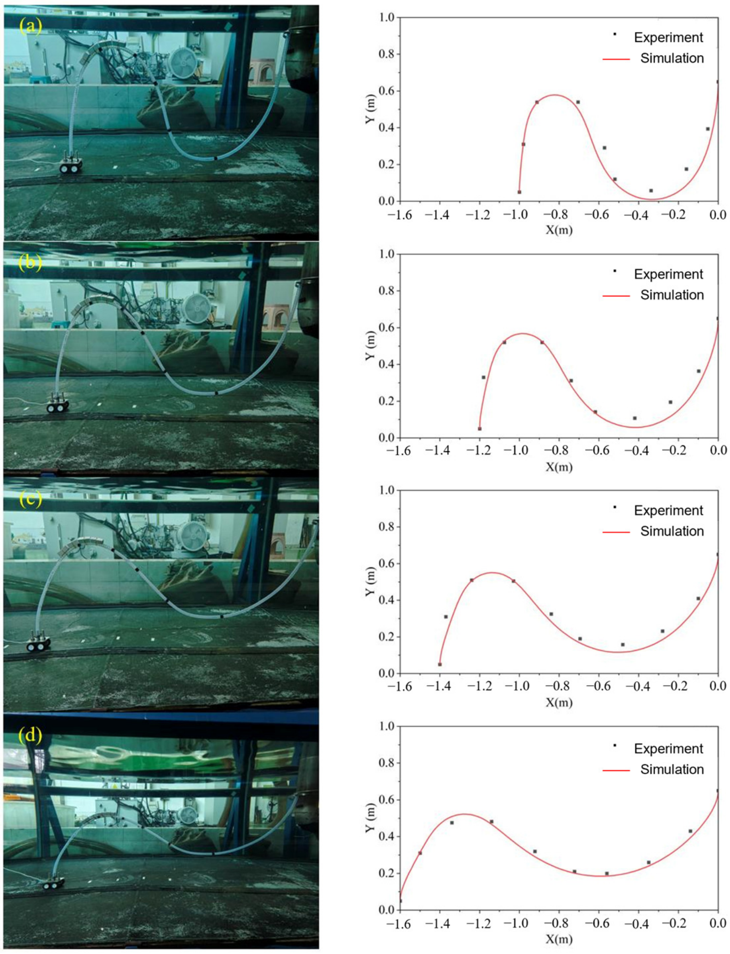

Figure 24. Comparative X–Z geometric profiles of test (scatter) and simulation (solid line) under Scheme 1 at four horizontal spacings (**a**–**d**).

With buoyancy blocks moving farther from the mining vehicle end (Schemes 2 and 3), buoyancy action points shift toward the hose mass center, lifting both arch crown and arch bottom elevation (Figures 25 and 26). At horizontal separation of 1.2 m, arch crown heights of the three schemes are 0.54 m, 0.73 m and 0.82 m, respectively, with decelerating elevation growth. Numerical simulations can reproduce the main geometric variation trends under different buoyancy layouts, while point-wise local deviations exist, as shown in Table 9, which are attributed to manufacturing imperfection, optical refraction and manual coordinate extraction errors in tank tests. Minor discrepancies arise from initial hose torsion, tiny tank bottom slope, optical refraction of glass walls, manual coordinate extraction error and incomplete similarity of bending stiffness/buoyancy distribution. The scaled test is proven capable of validating qualitative geometric evolution laws of flexible hoses.

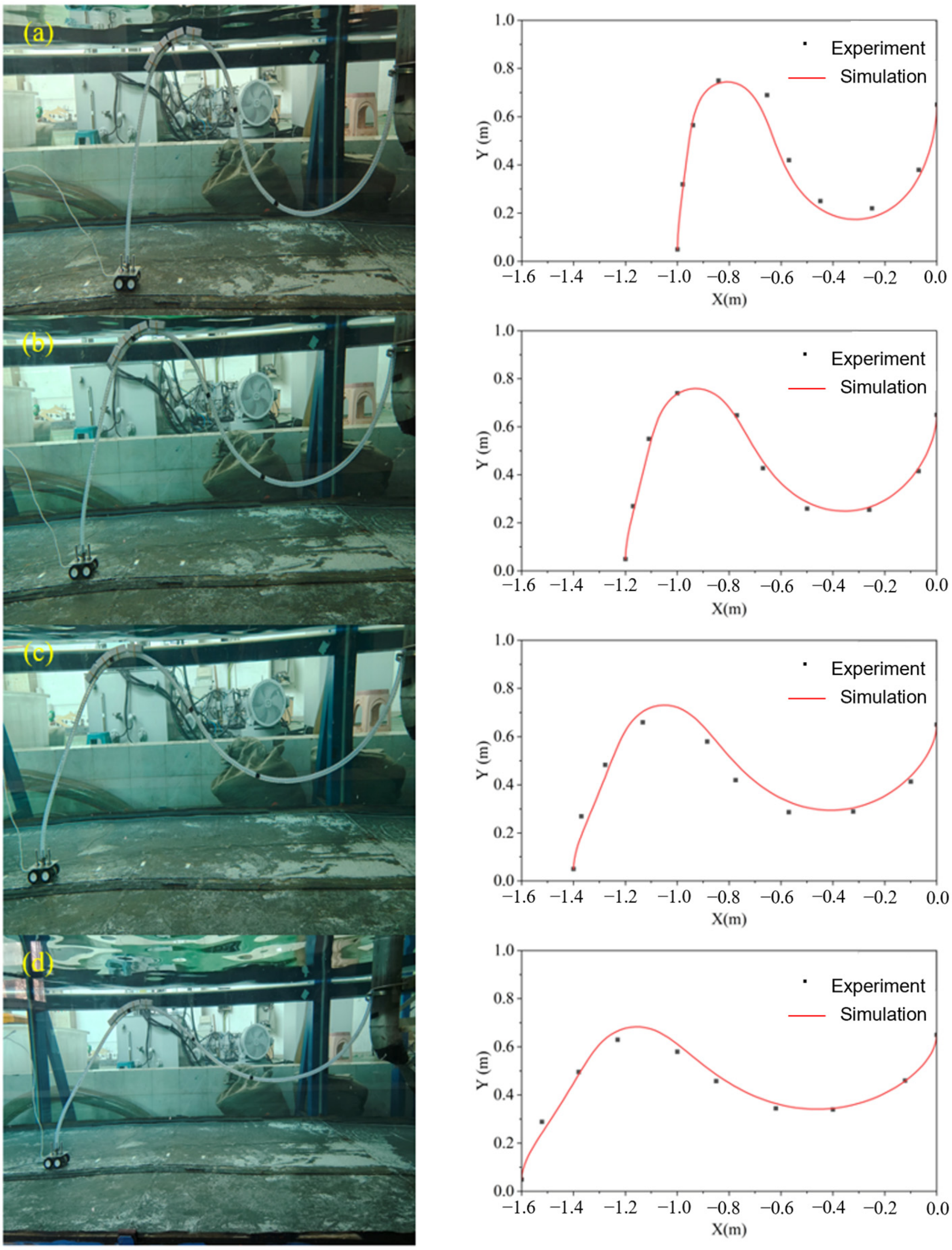

Figure 25. Comparative geometric profiles of test and simulation under buoyancy Scheme 2 at four horizontal spacings (**a**–**d**).

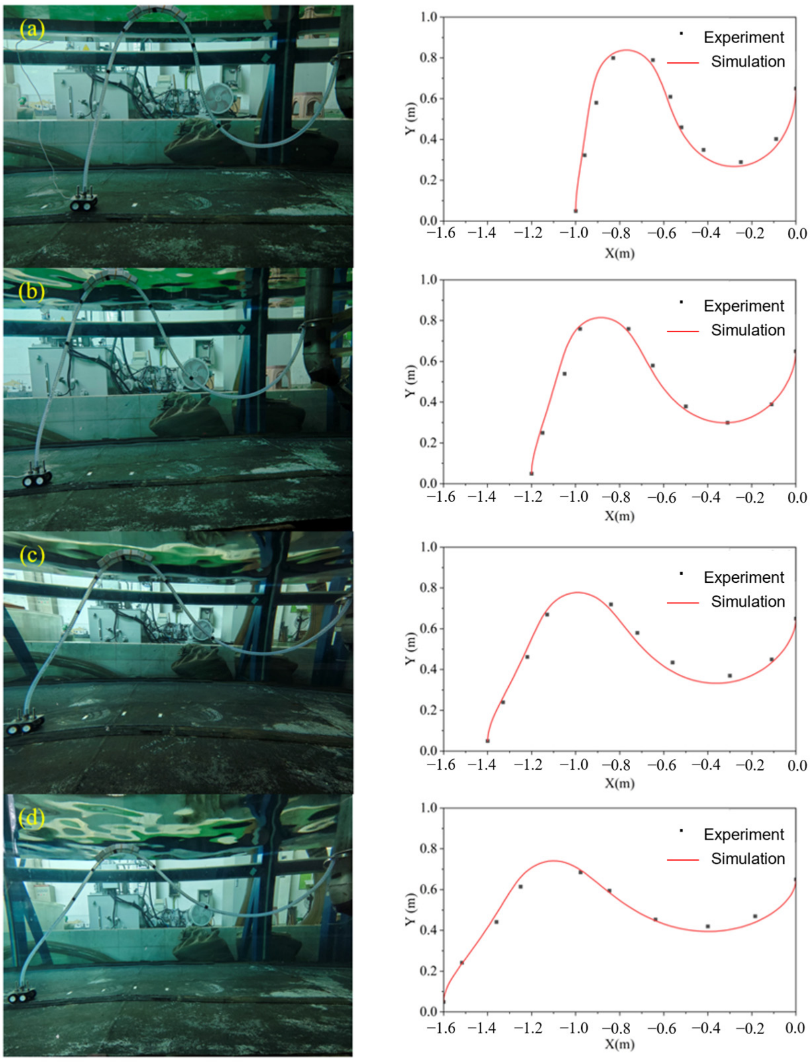

Figure 26. Comparative geometric profiles of test and simulation under buoyancy Scheme 3 at four horizontal spacings (**a**–**d**).

Table 9. Comparison of X–Y coordinate data between test measurement and numerical simulation under Scheme 1 at horizontal spacing of 1.2 m.

Point	Experiment		Simulation	
	x (m)	**y (m)**	**x (m)**	**y (m)**
1	−1.2	0.05	−1.2	0.05
2	−1.18	0.33	−1.18	0.23
3	−1.07	0.52	−1.07	0.52
4	−0.88	0.52	−0.88	0.51
5	−0.74	0.31	−0.74	0.28
6	−0.62	0.14	−0.62	0.13
7	−0.42	0.11	−0.42	0.06
8	−0.24	0.19	−0.24	0.12
9	−0.1	0.36	−0.1	0.29
10	0	0.65	0	0.65

4.2. CFD–DEM Model Validation via Vertical Pipeline Benchmark Test

The CFD–DEM methodology is assessed against the published vertical pipe solid–liquid transport experiments of Liu et al. [39] (Figure 27). The benchmark rig uses a 9.2 m long transparent vertical pipe with an inner diameter of 100 mm and a bulk slurry velocity of 3 m/s. An equal-scale numerical model is constructed for three combinations of particle density and inlet solid volume fraction (Table 10). The comparison focuses on mean particle velocity and local solid volume fraction, which are the principal indicators used in the flexible hose analysis (Figure 28).

Table 10. Working conditions used for the vertical pipe CFD–DEM validation.

Working Condition	Particle Density (kg/m^3)	Inlet Solid Volume Fraction
1	2450	0.06
2	2450	0.09
3	3600	0.06

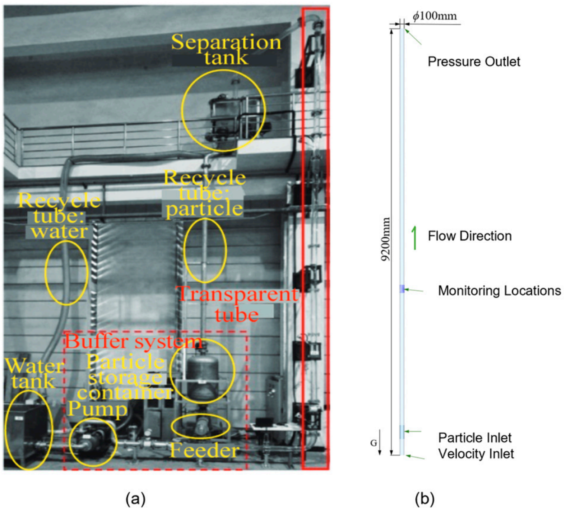

Figure 27. Vertical pipe benchmark: (**a**) experimental facility reported in [39]; (**b**) corresponding CFD–DEM model.

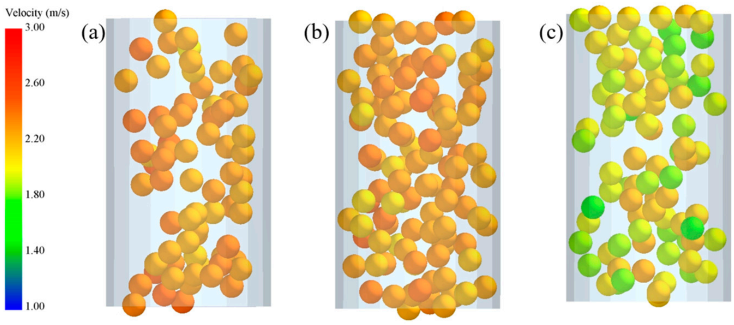

Figure 28. Particle-velocity fields for the three vertical pipe validation conditions (**a**–**c**).

It can be observed in Table 11 that all predicted particle velocities are slightly lower than experimental measurements, presenting systematic negative bias. This deviation may originate from particle–wall contact parameters, drag model selection or simplification of spherical particle assumption. If this bias also exists in curved hose calculations, it may slightly shift the predicted safe operating domain boundaries, which constitutes one limitation of the present model.

Table 11. Comparison of simulated and experimental mean particle velocity and local solid volume fraction.

Working Condition	Particle Velocity			Particle Concentration		
	Experiment [39]	Simulation	Error	Experiment [39]	Simulation	Error
1	2.6	2.34	−10%	0.086	0.080	−6.9%
2	2.57	2.32	−9.7%	0.101	0.109	7.9%
3	2.14	2.03	−5.1%	0.078	0.083	6.4%

5. Conclusions

1. Buoyancy section length and position jointly control hose suspension, curvature, and end effective tension. Layouts with insufficient coverage near the vehicle end (Schemes 1, 4, and 6) caused seabed contact, whereas layouts shifted too far toward the relay station (Schemes 3 and 8) produced negative end effective tension. Among the tested arrangements, Scheme 11, with buoyancy distributed from 0 to 0.6L, provided the preferred balance between suspension, positive end tension, curvature distribution, and vehicle loading.
2. Outward vehicle travel, particularly during turning at large separation, governed structural safety. The initial path exceeded the 18 kN longitudinal load limit, the 40.9 kN lateral load limit, and the 2 m minimum bending radius criterion. After path modification, the peak longitudinal, lateral, and vertical hose loads were 17.78, 22.38, and 22.44 kN, respectively, and all monitored bending radii remained above 2 m.
3. At the reference transport condition of 5 m/s and 10% solids, the 40 m configuration produced the strongest gravitational slip and concentration rebound near the lower bend, whereas the 197 m configuration promoted particle accumulation and a thicker moving bed in the ascending section. The 120 m case showed the smoothest velocity and concentration variation. Combining the structural and conveying criteria gives a recommended vehicle–relay horizontal separation of 80–160 m for the present model.
4. The scaled hose experiment reproduced the main configuration trends, with a mean absolute vertical coordinate error of 0.034 m for the reported Scheme 1 case. In the vertical pipe benchmark, the CFD–DEM predictions of mean particle velocity and local solid fraction differed from the experimental values by no more than 10%. These checks support comparative use of the numerical framework, while the derived operating domain remains conditional on the simplified particle representation, environmental assumptions, and one-way structural-to-flow coupling.

The multi-constraint evaluation framework and annular safe operating domain derived in this work can provide theoretical support for the preliminary design stage of deep-sea polymetallic nodule mining systems. The proposed workflow can assist engineers in determining the reasonable horizontal installation offset between the tracked mining vehicle and underwater relay station. Additionally, it offers reference constraints for path planning of mining vehicle travel trajectories. It should be kept in mind that these outputs are derived under idealized numerical assumptions. For real-site deployment, site-specific equipment parameters, seabed topography and ocean environmental conditions must be incorporated, and sufficient safety margins should be reserved before practical operation.

6. Limitations and Future Work

The 80–160 m spacing range and Scheme 11 buoyancy layout represent trade-off optimized solutions valid only for the specific equipment and working conditions in this paper, rather than universal industry standards. The core novelty of this work lies in establishing a quantitative engineering framework to convert both hose structural and internal flow limitations into travel path boundary criteria, distinguishing it from previous studies relying solely on mechanical analysis.

Research Limitations:

1. This study employs sequential one-way coupling between the structural and two-phase flow models. The hose geometry predicted by OrcaFlex is transferred to the CFD–DEM model, whereas the spatially nonuniform fluid–particle forces resolved by CFD–DEM are not fed back to update the hose deformation. Therefore, the influence of local two-phase flow-induced force fluctuations on the structural response is not

quantified in the present framework. This limitation may become more important at higher slurry velocities or solid concentrations.

2. All two-phase flow simulations in this paper are carried out under a single reference operating condition (bulk slurry velocity 5 m/s, solid volume fraction 10%). The derived safe horizontal spacing of 80–160 m is conditionally valid for this reference setup. Variations in conveying velocity and particle concentration will change particle slip magnitude, moving bed thickness and pressure loss inside the curved hose, which will shift the inner and outer boundaries of the safe operating domain. Therefore, this distance range cannot be directly generalized to arbitrary slurry transport parameters.
3. Waves, cross-currents, seabed irregularities, surface vessel offset, and vehicle–sediment dynamic interaction are not included in the present model. Waves and currents may increase transient hose loads and modify the load direction, whereas seabed irregularities may alter hose clearance and contact conditions. These effects would also break the horizontal isotropy assumed when the distance criterion is represented as an annular domain. Practical operating boundaries are therefore expected to be site-specific and should incorporate appropriate engineering safety margins.
4. The 1:100 pool test provides trend-level validation of hose geometry rather than full dynamic similarity with the prototype system. In addition, the structural simulations use a uniform segment length of 0.5 m. Because the minimum bending radius of 2 m is employed as a pass/fail criterion, the predicted curvature near the limiting condition remains subject to discretization uncertainty. A complete 0.25 m refinement calculation could not be completed within the present computational scope. A dedicated structural refinement study is therefore required in future work.

Future work should extend the framework to two-way structural–flow coupling, wave/current forcing, vehicle–sediment interaction, graded non-spherical particles, a wider velocity–concentration matrix, and refined structural discretization near critical bending regions.

Author Contributions: Conceptualization, Y.L. and K.J.; methodology, Y.L. and K.J.; software, Y.L. and K.J.; validation, Y.L. and Z.H.; formal analysis, Y.L.; investigation, Z.H.; resources, Z.H.; data curation, Y.L.; writing—original draft preparation, K.J. and Z.H.; writing—review and editing, Y.L.; visualization, K.J. and Z.H.; supervision, Y.L.; project administration, Y.L.; funding acquisition, Y.L. All authors have read and agreed to the published version of the manuscript.

Funding: This research was funded by the National Key Research and Development Program of China, grant number 2023YFC2811301.

Data Availability Statement: The data supporting the findings of this study are included in the article. Additional information is available from the corresponding author upon reasonable request.

Acknowledgments: The authors would like to thank the editors and anonymous reviewers for their careful work and thoughtful suggestions that have helped improve this paper substantially.

Conflicts of Interest: The authors declare no conflicts of interest.

References

1. International Energy Agency. *Global Critical Minerals Outlook 2025*; IEA: Paris, France, 2025.
2. Yu, M.; Deng, X.G.; Yao, H.Q.; Li, Y.G. The progress in the investigation and study of global deep-sea polymetallic nodules. *Geol. China* **2018**, *45*, 29–38. [CrossRef]
3. Zou, L.; Sun, J.Z.; Sun, Z.; Wang, J.Y.; Yang, Z.B. Deep-sea mining core technology in China: Current situation and prospects. *J. Harbin Eng. Univ.* **2023**, *44*, 708–716. [CrossRef]
4. Kang, Y.J.; Liu, S.J. Review on the Technology and Equipment Progress and the System Scheme of Deep-sea Mining. *J. Mech. Eng.* **2023**, *59*, 325–337. [CrossRef]

5. Wang, G.R.; Huang, Z.Q.; Zhou, S.W.; Fu, Q.; Zhong, L.; Zhu, D.M.; Liang, D.M.; Huang, C.H. Current Status and Development Direction of Deep-Sea Mineral Resource Exploitation Equipment. *Chin. J. Eng. Sci.* **2023**, *25*, 1–12. [CrossRef]
6. Kang, Y.J.; Liu, S.J. The Development History and Latest Progress of Deep-Sea Polymetallic Nodule Mining Technology. *Minerals* **2021**, *11*, 1132. [CrossRef]
7. Xu, H.L.; Chen, W.; Li, L.; Yang, F.Q. Spatial morphology and influencing laws of hydraulic conveying hoses under marine dynamic conditions for deep-sea mining. *J. Cent. South Univ.* **2023**, *30*, 3790–3807. [CrossRef]
8. Bai, Q.; Bai, Y. *Subsea Pipeline Design, Analysis, and Installation*; Gulf Professional Publishing: Houston, TX, USA, 2014.
9. Bai, Y. *Deepwater Flexible Risers and Pipelines*; John Wiley & Sons: Hoboken, NJ, USA, 2020.
10. Seyed, F.B.; Patel, M.H. Mathematics of flexible risers considering pressure and internal flow effects. *Mar. Struct.* **1992**, *5*, 121–150. [CrossRef]
11. Wang, G. A Study on the Spatial Configuration and Dynamic Characteristics of Mineral-Conveying Pipeline Systems During Deep-Sea Mining Operations. Doctoral Dissertation, Central South University, Changsha, China, 2009.
12. Oh, J.W.; Lee, C.H.; Kim, H.W. Arrangement Plan of Buoyancy Modules for the Stable Operation of the Flexible Riser in a Deep-Seabed Mining System. *Ocean Polar Res.* **2015**, *37*, 119–125. [CrossRef]
13. Xiao, F.Q. The Spatial Configuration Analysis and The Fluid–structure Coupling Mechanics Analysis of The Hose in Deep-ocean Mining System. Master's Thesis, Central South University, Changsha, China, 2012.
14. Peng, Y.; Xia, J.X.; Cao, B.; Ren, H.T.; Wu, Y. Spatial Configurations and Particle Transportation Parameters of Flexible Hose in Deep-sea Mining System. In Proceedings of the 25th ISOPE Ocean Mining and Gas Hydrates Symposium, Kona, HI, USA, 21–26 June 2015; pp. 186–190.
15. Chen, W.; Xu, H.L.; Wu, B.; Yang, F.Q.; Lin, P.; Hu, D. Spatial configuration and static characteristics of hoses in deep-sea ore conveying system. *Ocean Eng.* **2022**, *247*, 110649. [CrossRef]
16. Fu, Y. A Study on the Conveyance Characteristics of Hoses Used in Deep-Sea Mining. Master's Thesis, Minzu University of China, Beijing, China, 2019.
17. Fu, Y.; Cao, B.; Xia, J.X. Influence of Parameter Configuration of Hose Buoyancy for Deep-sea Mining System on the Stress State of Mining Vehicle. *Min. Metall. Eng.* **2019**, *39*, 15–18+23. [CrossRef]
18. Song, H.F.; Du, X.G.; Wang, S.; Du, C.Y. Parameter Sensitivity Analysis for Hose Configuration in Deep-sea Mining Conveying. *Shipbuild. China* **2020**, *61*, 154–163. [CrossRef]
19. Zou, L.; Guo, Q.; Jin, G.Q.; Zou, B.Y.; Jiang, H.Y. Mechanical characteristic analysis of flexible hoses for deep-sea mining in complex terrain based on ANCF. *J. Southeast Univ. Nat. Sci. Ed.* **2025**, *55*, 640–649. [CrossRef]
20. Amaechi, C.V.; Butler, H.O.; Beddu, S.B.; Syamsir, A.; Ja'e, I.A.; Reda, A.; Ju, X.Z. Parametric analysis on the global design of flexible riser under different environmental conditions using OrcaFlex. *PLoS ONE* **2024**, *19*, e0310360. [CrossRef] [PubMed]
21. Zhu, J.Y. Research and Construction of Digital Twin for Deep-Sea Mining Lifting System. Master's Thesis, Central South University, Changsha, China, 2024. [CrossRef]
22. Cao, Z.X.; Hu, P.; Li, W. *Mechanics of Sediment Movement*, 1st ed.; China Water & Power Press: Beijing, China, 2021.
23. Yoon, C.H.; Kwon, K.S.; Kwon, S.K. An experimental study on the flow characteristics of solid–liquid two-phase mixture in a flexible hose. In Proceedings of the 4th ISOPE Ocean Mining Symposium, Szczecin, Poland, 23–27 September 2001; pp. 122–126.
24. Yoon, C.H.; Lee, D.K. Flow Characteristics of Solid–Liquid Two-Phase Mixture in a Flexible Pipe. *Geosyst. Eng.* **2003**, *6*, 7–12. [CrossRef]
25. Yoon, C.H.; Lee, D.K.; Kwon, K.S.; Kwon, S.K.; Park, Y.C. The Effects of Pipe Curvature on the Flow Characteristics of Solid-liquid Two-phase Mixture in an Experimental Flexible Hose System. *Geosyst. Eng.* **2002**, *5*, 1–7. [CrossRef]
26. Parenteau, T.; Lemaire, A. Flow Assurance for Deep Ocean Mining—Pressure Requirement Through S-Shape Riser and Jumper. In Proceedings of the Offshore Technology Conference, Houston, TX, USA, 2–5 May 2011. OTC-21237-MS. [CrossRef]
27. Murai, M.; Yamamoto, M.; Uto, S.; Fujiwara, T. An Experimental Analysis of a Flexible Riser in Jumper Configuration. In Proceedings of the 30th ASME OMAE Conference, Rotterdam, The Netherlands, 19–24 June 2011; pp. 495–502.
28. Wang, Z.; Rao, Q.H.; Liu, S.J. Fluid-solid interaction of resistance loss of flexible hose in deep ocean mining. *J. Cent. South Univ.* **2012**, *19*, 3188–3193. [CrossRef]
29. Liu, L.; Gai, K.Y. Numerical Investigation on the Dynamics of Mixture Transport in Flexible Risers during Deep-Sea Mining. *J. Mar. Sci. Eng.* **2022**, *10*, 1842. [CrossRef]
30. Gai, K.Y.; Liu, L. Numerical study on hydraulic transportation of seabed ores through a hose. *Ocean Eng.* **2023**, *41*, 110–122. [CrossRef]
31. Wang, Y.; Zhang, R.; Chen, L.; Liu, Y.; Yu, L. Steady-state modeling and analysis of solid–liquid two-phase flow in vertical and flexible pipelines for deep-sea mining. *Ocean Eng.* **2025**, *341*, 122757. [CrossRef]
32. Nijun, Y.; Bin, C.; Jiangxin, X. Pressure loss of flexible hose in deep-sea mining system. In Proceedings of the 18th International Conference on Transport and Sedimentation of Solid Particles, Prague, Czech Republic, 11–15 September 2017; Volume 38, pp. 10–14.

33. Gong, S.; Xu, P. The influence of sea state on dynamic behaviour of offshore pipelines for deepwater S-lay. *Ocean Eng.* **2016**, *111*, 398–413. [CrossRef]
34. Jia, J.J.; Gu, J.J.; Huang, J.; Chen, L.L. Numerical simulation of loop formation in catenary risers on nonlinear uneven seabed. *Ocean Eng.* **2023**, *269*, 113480. [CrossRef]
35. Wang, M.H. *Development of Deep-Sea Solid Mineral Resources*; Central South University Press: Changsha, China, 2015.
36. Liu, Y.W.; Liu, S.J. Research on reflux in deep-sea mining pump based on DEM-CFD. *Mar. Georesour. Geotechnol.* **2020**, *38*, 744–752. [CrossRef]
37. Liang, K. A Study on Particle Impaction and Degradation in Two-Phase Flow Transport by Deep-Sea Mineral-Lifting Electric Pumps. Master's Thesis, Central South University, Changsha, China, 2022.
38. Zhang, M.; Zheng, H.; Shuang, Z.; Wei, W.; Li, X.Y. New Type of Discontinuous Mining System for Deep-Sea Polymetallic Nodules. *Min. Metall. Eng.* **2025**, *45*, 6–12. [CrossRef]
39. Liu, L.; Liu, J.C.; Li, X.; Xu, L.X.; Zhang, X.Z. Experimental Investigation on Vertical Hydraulic Transport of Ores in Deepsea Mining. *China Ocean Eng.* **2024**, *38*, 42–53. [CrossRef]

Disclaimer/Publisher's Note: The statements, opinions and data contained in all publications are solely those of the individual author(s) and contributor(s) and not of MDPI and/or the editor(s). MDPI and/or the editor(s) disclaim responsibility for any injury to people or property resulting from any ideas, methods, instructions or products referred to in the content.